

1 **It's Not Easy Being Green: Kinetic Modeling of the**
2 **Emission Spectrum Observed in STEVE's Picket Fence**

3 **L. Claire Gasque¹, Reza Janalizadeh², Brian J. Harding¹, Justin D. Yonker³,**
4 **D. Megan Gillies⁴**

5 ¹Space Sciences Laboratory, University of California, Berkeley

6 ²Department of Electrical Engineering, The Pennsylvania State University

7 ³The Johns Hopkins University Applied Physics Laboratory

8 ⁴Physics and Astronomy Department, University of Calgary

9 **Key Points:**

- 10 • Local parallel electric fields quantitatively replicate observed picket fence spectra
11 without requiring particle precipitation.
12 • At 110 km, parallel electric field strengths between 40 and 70 Td (~80 to 150 mV/m
13 at 110 km) reproduce observed picket fence spectra.
14 • Quantitative connections between electrodynamics and observable picket fence emis-
15 sions offer goalposts for future models and experiments.

Corresponding author: L. Claire Gasque, lccgasque@berkeley.edu

Abstract

Recent studies suggest that, despite its aurora-like appearance, the picket fence may not be driven by magnetospheric particle precipitation but instead by local electric fields parallel to Earth’s magnetic field. Here, we evaluate the parallel electric fields hypothesis by quantitatively comparing picket fence spectra with the emissions generated in a kinetic model driven by parallel electric fields in a realistic neutral atmosphere. We find that sufficiently large parallel electric fields can reproduce the observed ratio of N_2 first positive to oxygen green line emissions, without producing N_2^+ first negative emissions. At a typical picket fence altitude of 110 km, parallel electric fields between 40 and 70 Td (~ 80 to 150 mV/m at 110 km) replicate the observations. These findings establish a quantitative connection between electrodynamics and observable picket fence emissions, offering verifiable targets for future models and experiments.

Plain Language Summary

The ‘picket fence’ is a captivating visual phenomenon featuring vibrant green streaks often seen below the rare purpleish-white arc called STEVE. It occurs in the subauroral sky, closer to the equator than the auroral oval, raising questions about whether it is a type of aurora or a separate phenomenon. Recent hypotheses propose that strong electric fields aligned with Earth’s magnetic field might be responsible for creating the picket fence, setting it apart from traditional auroras caused by energetic particles from space colliding with the upper atmosphere. In this study, we compare optical observations of the picket fence to a detailed calculation of the emissions produced by parallel electric fields in the upper atmosphere. The results show that large parallel electric fields can indeed replicate the observed picket fence phenomenon. These findings offer important targets for future picket fence models and experiments. This research demonstrates that the picket fence serves as a valuable testing ground for understanding kinetic chemistry and electrodynamics in Earth’s upper atmosphere.

1 Introduction: Debate Over the Picket Fence’s Origin

STEVE (Strong Thermal Emission Velocity Enhancement) is a rare ionospheric optical phenomenon characterized by a narrow mauve arc extending thousands of kilometers east/west across the subauroral sky (MacDonald et al., 2018). Below STEVE, vibrant green streaks known as the “picket fence” often appear after the mauve arc develops and occasionally persist after it fades (Yadav et al., 2021; Martinis et al., 2022; Nishimura et al., 2023). STEVEs are associated with strong sub-auroral ion drifts (SAIDs) (Archer, Gallardo-Lacourt, et al., 2019), but the mechanism behind the optical emissions is still debated (Harding et al., 2020).

Early studies proposed that picket fence emissions, like auroras, are generated by magnetospheric particle precipitation (MacDonald et al., 2018; Chu et al., 2019; Nishimura et al., 2019; Bennett & Bourassa, 2021). Like green aurora, the picket fence primarily consists of 557.7 nm green line (GL) emissions (Gillies et al., 2019). However, the picket fence spectrum published by Gillies et al. (2019) and reanalyzed by Mende et al. (2019) lacks 427.8 nm N_2^+ first negative ($N_2^+ 1N$) emissions, which are ubiquitous and prominent in auroral spectra. The absence cannot be explained by a local N_2 depletion, as Mende et al. (2019) also detect N_2 first positive ($N_2 1P$) emissions. Instead, Mende et al. (2019) proposed that picket fence emissions result from local electrons energized to between 7.35 eV (sufficient for $N_2 1P$ emissions) and 18.75 eV (sufficient for $N_2^+ 1N$ emissions). They did not describe how electrons might be locally accelerated to such energies.

Recent studies by Lynch et al. (2022) and Mishin and Streltsov (2022) proposed that picket fence emissions arise when electric fields parallel to Earth’s magnetic field energize local electrons. Lynch et al. (2022) demonstrate that ionospheric conductance

65 gradients created by SAIDs create large field-aligned currents, potentially triggering tearing-
 66 mode instabilities similar to those observed in rayed auroral arcs. Mishin and Streltsov
 67 (2022) simulated the ionospheric feedback instability (IFI) under SAID conditions. Their
 68 approximate solution of the Boltzmann equation indicated that parallel electric fields gen-
 69 erated by the IFI might be sufficient to produce the suprathermal electron population
 70 responsible for the picket fence emissions. However, they did not conclusively demon-
 71 strate whether this electron population quantitatively reproduces the observed picket fence
 72 spectral features.

73 In this study, we conduct kinetic calculations in a realistic neutral atmosphere from
 74 100 to 180 km, considering all relevant electron-neutral collisions. Additionally, we com-
 75 pare our calculated spectral features with those in ground-based picket fence observa-
 76 tions. Our findings demonstrate that local parallel electric fields quantitatively replicate
 77 observed picket fence spectra without requiring particle precipitation. Estimating the
 78 magnitude of these fields provides a benchmark for future models and observations. This
 79 work enables a quantitative comparison between electrodynamic models and observable
 80 optical emissions, which previous studies have not achieved.

81 2 Picket Fence Spectral Observations

82 The Transition Region Explorer (TREx) Spectrograph in Lucky Lake, Saskatchewan
 83 captures visible (385-801 nm) spectral data for a narrow ($\sim 2.1^\circ$ wide) North/South lat-
 84 itudinal slice of the sky. For additional details about TREx's operation and calibration,
 85 refer to Gillies et al. (2019). On April 10, 2018, the same night as the observations pre-
 86 sented by Gillies et al. (2019), TREx observed the picket fence several times between 6:28
 87 and 8:00 UT. Figure 1(a) presents a keogram of the observations, showing the total ob-
 88 served luminosity as a function of elevation angle and time. Thin horizontal features brighter
 89 than the background are stellar contamination.

90 Figure 1(b) displays a keogram of the GL portion of the spectrum (555.2-560.7 nm).
 91 Picket fence spectra are identified following the method in Gillies et al. (2019) and Mende
 92 et al. (2019). We fit a Gaussian function to the GL luminosity with respect to elevation
 93 angle at each time step, determining the elevation angle at the peak brightness μ and
 94 the standard deviation σ . For luminosity curves with a defined peak at least 200 R above
 95 background luminosity, the picket fence spectrum is selected at the elevation bin μ , while
 96 background spectra are selected at elevation bins $\pm 3\sigma$ away from μ . Picket fence spec-
 97 tra with stellar contamination are discarded, and contaminated background spectra are
 98 replaced by neighboring uncontaminated pixels. Figure 1(c) displays the extracted picket
 99 fence spectra (black dots) and the selected poleward (blue triangles pointing up) and equa-
 100 torward (red triangles pointing down) backgrounds between 6:49 and 7:00 UT.

101 The picket fence is expected to lie between 97 and 150 km and be approximately
 102 aligned with the magnetic field (Archer, St.-Maurice, et al., 2019; Semeter et al., 2020).
 103 The black dotted line in Figure 1(d) represents the look direction up the magnetic field,
 104 calculated using the International Geomagnetic Reference Field, Version 13 (IGRF13)
 105 (Wardinski et al., 2020; Michael, 2021). Our kinetic model described in Section 3 assumes
 106 emissions originate from a uniform source at a single altitude, avoiding assumptions about
 107 the vertical parallel electric field profile. Consequently, select picket fence spectra closer
 108 to the horizon, away from the magnetic field look direction, to reduce the vertical pro-
 109 file intersected by the line-of-sight. Specifically, we use 45 uncontaminated picket fence
 110 spectra observed between 6:45 and 7:30 UT, all with elevation angles between 131° and
 111 142° . Figure 1(d) depicts the picket fence observation geometry at 6:52 UT. The observed
 112 GL luminosity is projected onto an arc at an arbitrary altitude, and the equatorward
 113 and poleward picket fence boundaries are marked by solid red and blue lines, respectively.
 114 The observed picket must lie within the wedge formed by these boundaries. Assuming
 115 that the picket fences are 5-25 km wide latitudinally (Liang, Zou, et al., 2021), we es-

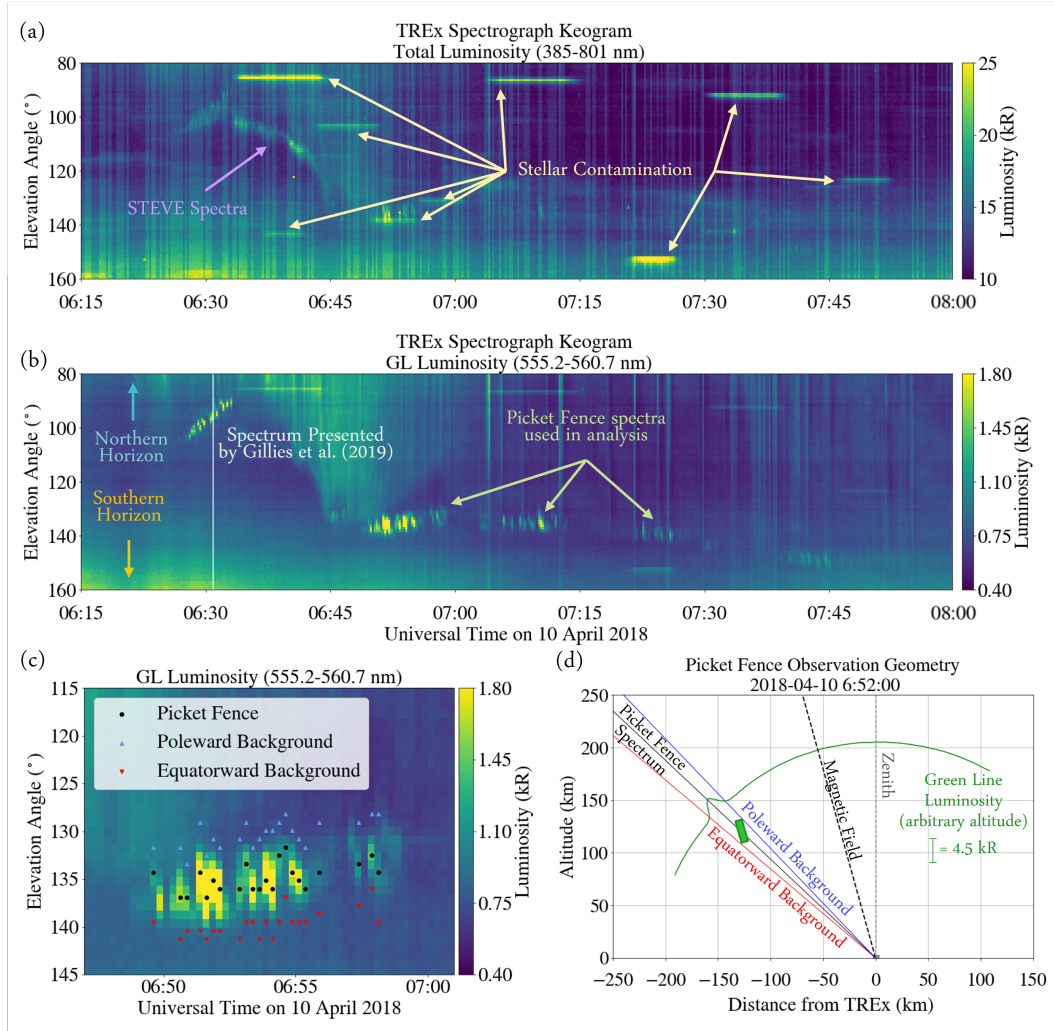


Figure 1. (a) Keogram of total TReX luminosity between 6:15 and 8:00 UT on April 10, 2018, showing STEVE emissions and stellar contamination. (b) Keogram of TReX GL observations (555.2-560.7 nm) during the same period, highlighting the picket fence observations. (c) Picket fence and background spectra extracted between 6:49 and 7:00 UT. Some spectra were removed due to stellar contamination. See text for details of selection process. (d) Approximate observation geometry for picket fence observed at 6:52 UT. The sample picket shown is only a representation as the altitude of the emissions is unknown.

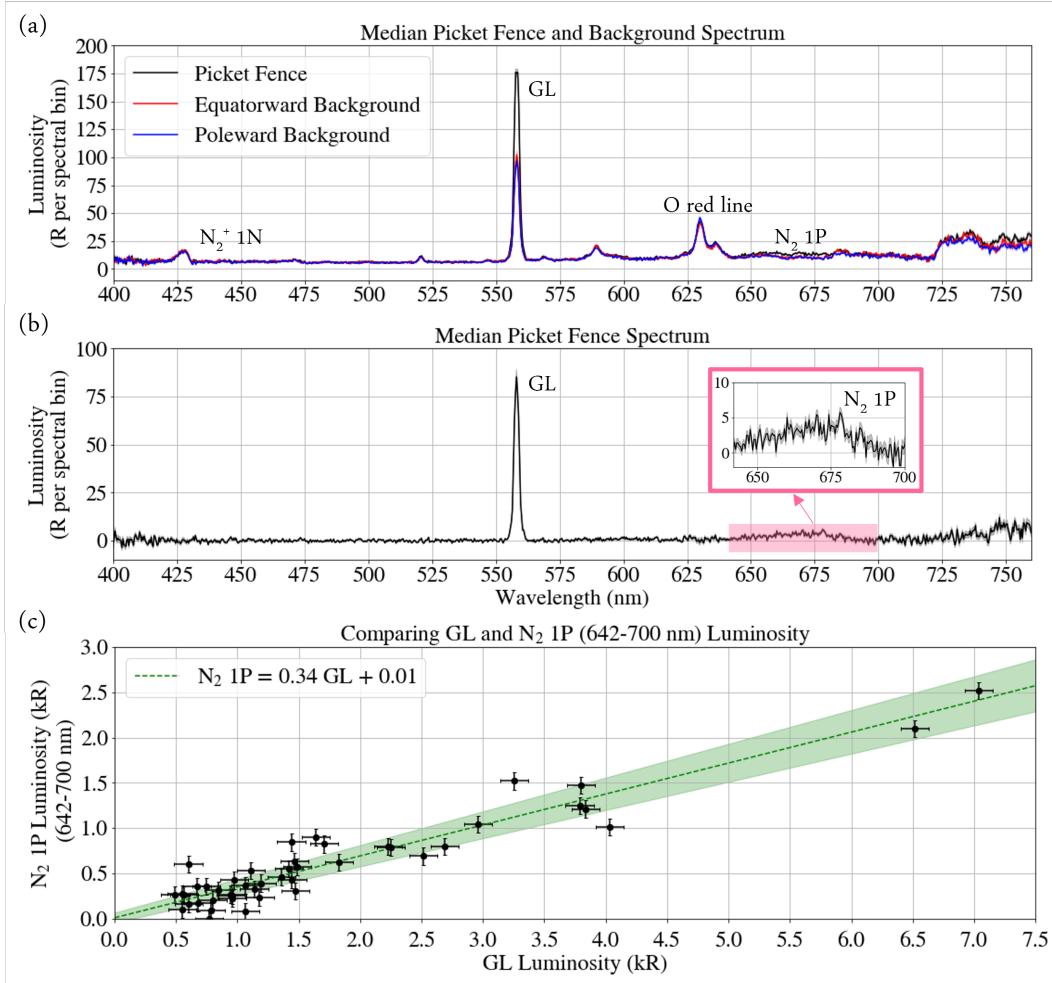


Figure 2. (a) Median picket fence spectrum (black) and poleward (blue) and equatorward (red) background spectra. (b) Median picket fence spectrum after background subtraction. Inset: N_2 1P spectrum (642-700 nm). (c) Ratio of N_2 1P (642-700 nm) to GL luminosity from the TReX observations, scaled to account for atmospheric transmission.

116 timate that the line-of-sight cuts through no more than 25 km of the altitudinal profile
 117 for the selected observations, with most examples cutting through no more than 15 km.
 118 Due to these observational constraints, our quantitative results in Section 4 represent
 119 vertical averages over a maximum of 25 km.

120 We isolate individual picket fence spectra by subtracting the average of their pole-
 121 ward and equatorward background spectra. The error in each spectrum is determined
 122 by propagating the standard deviation variations in the background spectra at each wave-
 123 length through the background subtraction. Figure 2(a) shows the median picket fence
 124 and background spectra, while Figure 2(b) displays the median background-subtracted
 125 picket fence spectrum. The dominant features are the 557.7 nm GL and the N_2 1P band
 126 system, while the 427.8 nm N_2^+ 1N emissions observed in the background spectra are ab-
 127 sent in the picket fence spectrum, consistent with the findings of Mende et al. (2019).

128 Instead of directly comparing the absolute observed brightness to our model results,
 129 which requires assuming the picket fence’s latitudinal width and the local electron den-

130 sity, we focus on comparing the ratio of N₂ 1P and GL luminosities. For the GL, we cal-
 131 culate the luminosity between 555.2-560.7 nm, accounting for the GL’s spectral width.
 132 For N₂ 1P, we calculate the luminosity between 642 and 700 nm. Although N₂ 1P emis-
 133 sions extend to infrared (IR) wavelengths and TREx’s range extends to 800 nm, we only
 134 consider this part of the spectrum to avoid larger errors near the edge of TREx’s obser-
 135 vational band and complications from O₂ atmospheric absorption above 700 nm.

136 To quantitatively compare the in situ ratio of N₂ 1P to GL emissions, we must con-
 137 sider atmospheric transmission between the emission source and TREx. We apply an at-
 138 mospheric transmission profile from Figure 1(a) of Morrill et al. (1998), which corresponds
 139 to a source at 65 km observed from the ground at an elevation angle of 40°, similar to
 140 our observations. While the picket fence occurs at higher altitudes, most atmospheric
 141 scattering and absorption occur in the lower atmosphere, so this difference is assumed
 142 to be negligible (Meier, 1991). According to Morrill et al. (1998), the transmittance at
 143 557.7 nm for GL is 0.42, and the average transmittance for N₂ 1P between 642 and 700
 144 nm is 0.53. This results in a transmittance ratio of ~ 1.26 between the two features.

145 We perform linear regression on the data using the model $y = \alpha x + \beta$, where y
 146 represents the N₂ 1P luminosities, x represents the GL luminosities, α represents the lu-
 147 minosity ratio, and β represents the intercept. Using a Bayesian approach to linear re-
 148 gression with errors in both variables, following the method described by Gull (1989),
 149 we estimate the best-fit parameters and their errors. Our analysis yields $\alpha = 0.34 \pm$
 150 0.03 and $\beta = 9.4 \pm 56.9$ R. These results are displayed in Figure 2(c). Mende et al. (2019)
 151 conducted a similar analysis without considering transmission effects and found an N₂
 152 1P to GL ratio of 0.39. If we neglect transmission effects, our ratio is $\alpha = 0.43 \pm 0.04$,
 153 which is consistent with Mende et al. (2019)’s findings. We note that the ratio for green
 154 aurora is 0.72, significantly different from our picket fence results (Vallance Jones, 1974).

155 3 Kinetic Modeling of Emissions Driven by Parallel Electric Fields

156 Successful models of mechanisms generating the picket fence must be able to achieve
 157 the observed ratio of 0.34 between N₂ 1P (642-700 nm) and GL emissions while keep-
 158 ing N₂⁺ 1N emissions undetectable. Here, we explore whether a kinetic model driven solely
 159 by parallel electric fields can replicate these features. The following subsections outline
 160 the modeling process, including determining the atmospheric and ionospheric inputs, an-
 161 alyzing the effect of a parallel electric field on the local electron energy distribution func-
 162 tion (EEDF), and employing steady-state kinetic modeling to calculate volume emission
 163 rates (VERs) of excited atomic and molecular states. Figure 3 summarizes the model-
 164 ing process.

165 3.1 Model Inputs: Atmospheric and Ionospheric Conditions

166 We use established models to characterize atmospheric, ionospheric, and magnetic
 167 field conditions for the time, location, and geomagnetic conditions of the TREx obser-
 168 vations described in Section 2. The Naval Research Laboratory’s Mass Spectrometer In-
 169 coherent Scatter Radar (MSIS) model version 2.1 provided profiles of neutral temper-
 170 ature and densities for eight neutral species (Picone et al., 2002; Emmert et al., 2021,
 171 2022; Lucas, 2023). Ionospheric electron density and temperature profiles were taken from
 172 the International Reference Ionosphere 2016 (IRI16) (Bilitza et al., 2017; Ilma, 2017).
 173 The magnitude of the magnetic field was obtained from IGRF13 (Wardinski et al., 2020;
 174 Michael, 2021). The resulting profiles are shown in Figure S1 of the Supplemental In-
 175 formation.

176 Using these profiles assumes that picket fence conditions are similar to climatolog-
 177 ical conditions. However, STEVE and the picket fence are associated with intense SAIDs
 178 (MacDonald et al., 2018; Archer, Gallardo-Lacourt, et al., 2019), rare events character-

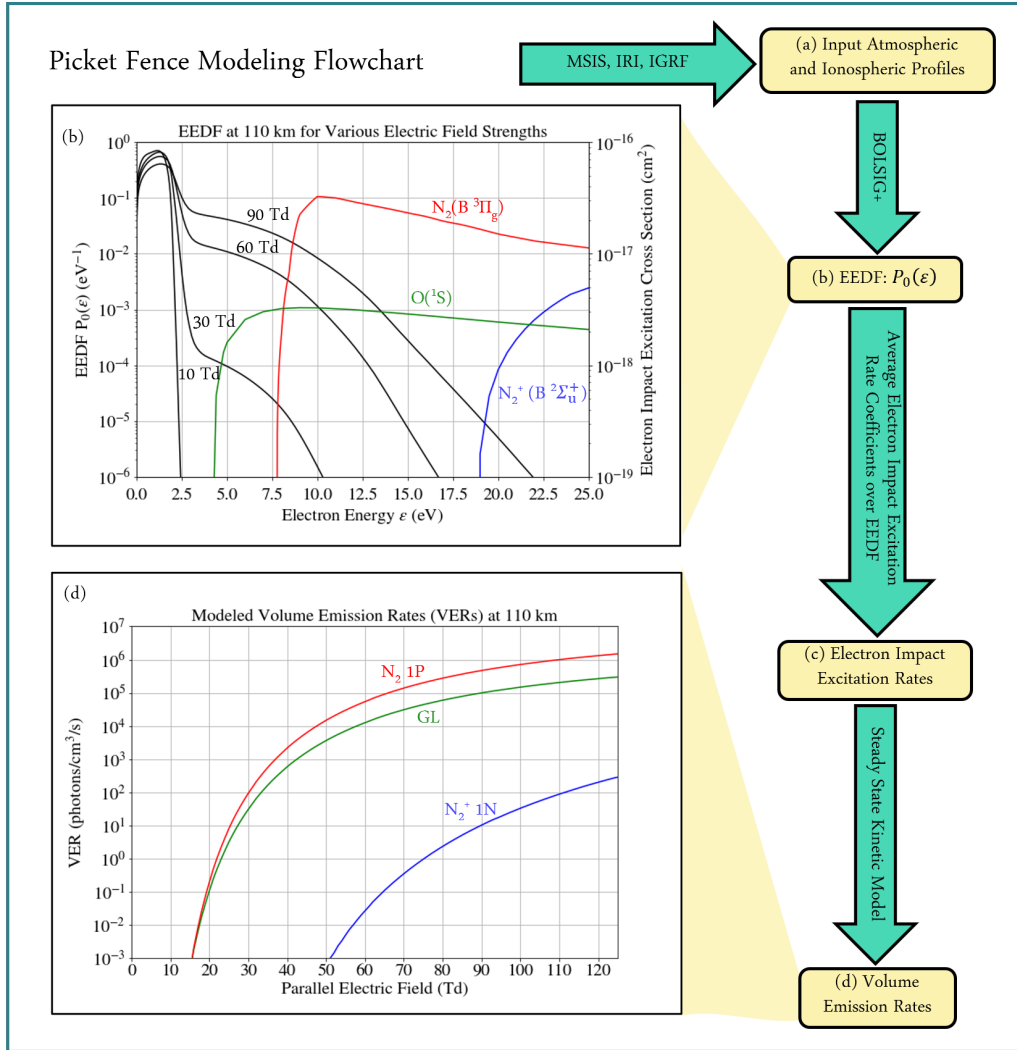


Figure 3. Modeling process flowchart of steps (a) - (d), with subfigures to further elucidate steps (b) and (d). (b) EEDFs at 110 km for different parallel electric field strengths, overlaid with electron impact excitation cross sections for $\text{O}(^1S)$, $\text{N}_2(B^3\Pi_g)$, and $\text{N}_2^+(B^2\Sigma_u^+)$. (d) VERs at 110 km for GL, N_2 1P, and N_2^+ 1N calculated with the steady state kinetic model.

179 ized by narrow channels of hot, fast-flowing, and depleted plasma (Liang, St-Maurice,
 180 & Donovan, 2021). Although IRI does not replicate these conditions, the ratio between
 181 N₂ 1P (642-700 nm) and GL emissions is independent of electron density, so this does
 182 not affect our results. Additionally, Mishin and Streltsov (2022) suggested that SAID
 183 conditions may lead to neutral upwelling, which is not captured by MSIS and which may
 184 decrease the O/N₂ ratio at picket fence altitudes. Doubling the O/N₂ ratio input in our
 185 model introduces changes on the order of 25% to our electric field magnitude predictions
 186 which, while significant, do not alter our qualitative findings.

187 3.2 Calculating EEDFs and Electron Impact Excitation Rates

188 We used BOLSIG+ (version 12/2019) (Hagelaar & Pitchford, 2005) to solve the
 189 Boltzmann equation, quantifying changes in the EEDF with altitude and parallel elec-
 190 tric field strength. BOLSIG+ calculates a steady-state solution under a uniform elec-
 191 tric field, so time-dynamics, non-local electron transport, and electric field gradients are
 192 not considered. Additionally, we neglect the effect of Coulomb collisions (Gurevich, 1978).
 193 Fractional densities of N₂, O₂, and O were obtained from MSIS, while electron impact
 194 collisional cross sections of N₂, O₂, and O were obtained from Phelps and Pitchford (1985),
 195 Lawton and Phelps (1978), and Laher and Gilmore (1990), respectively.

196 We consider altitudes between 100 and 180 km, where the 180 km upper bound is
 197 well above the expected picket fence altitude (Archer, St.-Maurice, et al., 2019). The 100
 198 km lower bound approximately marks the division between the atmospheric collisional
 199 regime, where collisions among excited states are important, and the radiational regime
 200 dominated by electron impact excitation (Yonker & Bailey, 2020). We considered reduced
 201 parallel electric fields ranging from $E/N = 0$ to 120 Townsend (Td) where E is the elec-
 202 tric field in V/m, N is the neutral density in m⁻³, and 1 Td = 10⁻²¹ V m². The up-
 203 per limit corresponds to the breakdown field E_k in conventional air at low altitudes (Raizer,
 204 1991, p. 137).

205 Figure 3(b) displays EEDFs at 110 km for parallel electric fields of 10, 30, 60, and
 206 90 Td (equivalent to 20, 60, 115, and 170 mV/m at 110 km, respectively). The figure
 207 highlights several electron impact collisional cross sections: O(¹S) in green, N₂(^B3Π_g)
 208 in red, and N₂⁺(^B2Σ_u⁺) in blue. Stronger electric fields stretch the tail of the EEDF to
 209 higher energies, enhancing high-energy electron populations and increasing electron im-
 210 pact excitation rate coefficients.

211 3.3 Calculating Volume Emission Rates

212 To calculate theoretical VERs for N₂ 1P, GL, and N₂⁺ 1N emissions, we implement
 213 a steady-state kinetic model which accounts for additional production and loss processes
 214 for excited states of N₂ and O. For N₂ 1P emissions, produced through relaxation of the
 215 N₂(^B3Π_g) state to the N₂(^A3Σ_u⁺) state, we account for radiative cascade from higher
 216 N₂ triplet states (Meier, 1991). For GL emissions, produced via relaxation of the O(¹S)
 217 state to the O(¹D) state, we incorporate additional O(¹S) production via O quenching
 218 of N₂(^A3Σ_u⁺). We also consider additional quenching of O(¹S) and N₂(^A3Σ_u⁺) by O,
 219 O₂, and NO. N₂⁺ 1N emissions occur via relaxation of N₂⁺(^B2Σ_u⁺) state to the ground
 220 state following electron impact ionization (Shemansky & Liu, 2005). For more details
 221 about these calculations, see Section S1 of the Supplementary Information.

222 We compared these calculated VERs to those obtained by inputting our electron
 223 impact excitation rates into Yonker and Bailey (2020)'s model, which includes interac-
 224 tions between individual N₂ excited states and resolves the vibrational states of N₂. Be-
 225 tween 105 and 150 km, the difference in the N₂ 1P to GL emission ratio between our model
 226 and Yonker and Bailey (2020)'s is below 15%, demonstrating excellent agreement. At
 227 lower altitudes, where the collisional regime dominates, the difference remains below 40%.

228 Figure 3(d) presents the modeled VERs for N_2 1P, GL, and N_2^+ 1N at 110 km
 229 as a function of parallel electric field strength. The VERs are directly proportional to elec-
 230 tron density, which may be depleted under SAID conditions, so the actual VERs may
 231 be reduced if the picket fence lies within the depleted channel. However, the ratio be-
 232 tween these VERs remains independent of the electron density.

233 4 Comparison with Observations

234 Figures 4(a) and 4(b) present calculated N_2 1P to GL VER ratios for parallel elec-
 235 tric fields in units of Td and mV/m, respectively, where the N_2 1P spectrum has been
 236 truncated to only include the 642-700 nm portion. The complete picket fence N_2 1P spec-
 237 trum has never been measured, so we use an estimated scaling factor of $\sim 8\%$ determined
 238 from modeling of the N_2 1P spectrum in aurora, presented in Table 4.12 of Vallance Jones
 239 (1974). The observed ratio and its data-driven uncertainty are indicated in Figures 4(a)
 240 and (b) by the black dotted lines and shaded regions, respectively. At 110 km, the ob-
 241 served N_2 1P (642-700 nm) to GL ratio is reproduced for parallel electric field strengths
 242 between 40 and 70 Td (~ 80 to 150 mV/m at 110 km). Assuming a picket fence width
 243 of ~ 10 km, a uniform emission source, and electron densities given by IRI, this corre-
 244 sponds to GL luminosities between 0.5 and 31 kR, consistent with observations.

245 If the N_2 ($B^3\Pi_g$) vibrational distribution differs between aurora and the picket fence,
 246 the shape of the N_2 1P spectrum may also differ. A test was performed in which our elec-
 247 tron impact excitation rates were inputs to Yonker’s vibrationally-resolved model; the
 248 results suggested the 642-700 nm portion may account for 12-14% of the total N_2 1P spec-
 249 trum. Adopting this higher scale factor leads to a $\sim 50\%$ reduction in our predicted par-
 250 allel electric field strength at 110 km. Obtaining a picket fence N_2 1P spectrum extend-
 251 ing into the IR would enhance confidence in our quantitative estimates of parallel elec-
 252 tric field strength, although our qualitative findings remain unchanged.

253 The calculated N_2^+ 1N to GL VER ratios are presented in Figure 4(c). Even for
 254 large parallel electric field strengths, this ratio remains below 10^{-3} at picket fence alti-
 255 tudes, undetectable by the TREx spectrograph for even the brightest picket fence events.
 256 Thus, we find that parallel electric fields of realistic magnitudes will not produce observ-
 257 able N_2^+ 1N emissions.

258 These results demonstrate that a model driven by parallel electric fields can repro-
 259 duce all of the key picket fence spectral features at picket fence altitudes, strongly sup-
 260 porting parallel electric fields as a plausible driving mechanism for picket fence emissions.

261 5 Discussion and Conclusion

262 This study provides quantitative evidence that spectral features of picket fence emis-
 263 sions can be reproduced by a kinetic model driven solely by parallel electric fields, of-
 264 fering a substantiated alternative to magnetospheric precipitation, which lacks support-
 265 ing spectral evidence. As a reference point for future observations and modeling, we find
 266 that at 110 km 40-70 Td (~ 80 -150 mV/m at 110 km) parallel electric fields produce observationally-
 267 consistent picket fence spectra. The developed kinetic and chemical modeling tools could
 268 be used as post-processors or two-way coupled into global or regional MHD models to
 269 simulate the picket fence or its potential connections to other subauroral phenomena such
 270 as SAIDs, STEVE, or stable auroral red (SAR) arcs (Gallardo-Lacourt et al., 2021; Hard-
 271 ing et al., 2020; Martinis et al., 2022; Gillies et al., 2023; Liang, St-Maurice, & Dono-
 272 van, 2021).

273 While we have demonstrated the plausibility of parallel electric fields as a driving
 274 mechanism for the picket fence, further measurements are essential to validate or chal-
 275 lenge this hypothesis. Our modeling demonstrates that parallel electric fields of mag-

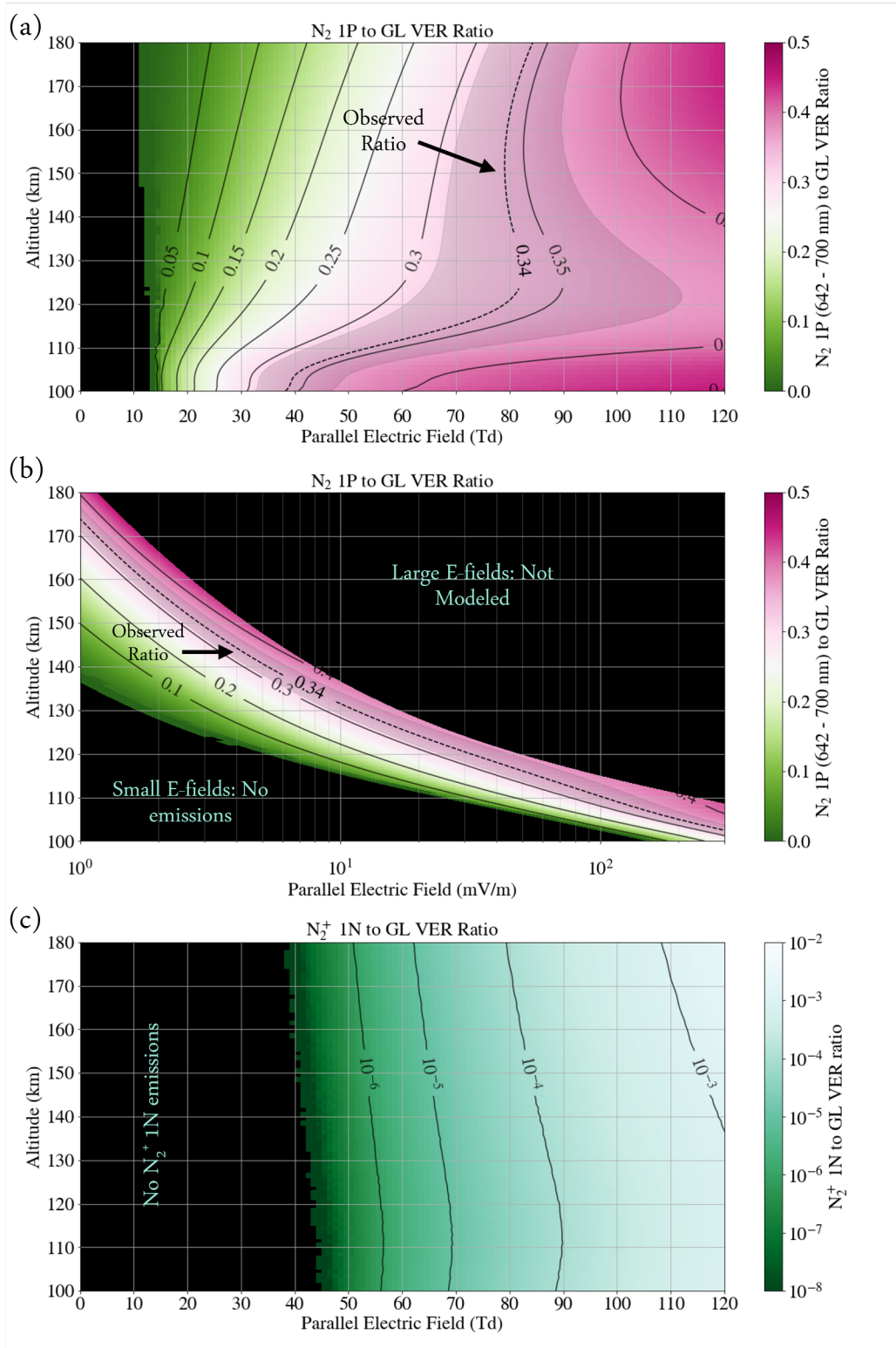


Figure 4. (a) Calculated N₂ 1P (642-700 nm) to GL VER ratios. Observed luminosity ratios and margins of error are indicated by the black dotted line and shaded region, respectively. (b) The same as (a), but with parallel electric field strength in mV/m. (c) Calculated N₂⁺ 1N (421-431 nm) to GL VER ratios.

276 nitudes considered here would not generate observable N_2^+ 1N emissions. Therefore, any
 277 future observations of N_2^+ 1N emissions in a picket fence would prompt reassessment of
 278 this mechanism. Furthermore, Section S2 describes an extension of our model to pre-
 279 dict ultraviolet (UV) spectral features of the picket fence, which could be confirmed by
 280 space-based observations. For the brightest picket fence events, we find that N_2 Vegard-
 281 Kaplan (VK) and Lyman-Birge-Hopfield (LBH) emissions could be promising observa-
 282 tional targets. However, N_2 Second Positive (2P) bands and 1356 Å atomic oxygen emis-
 283 sions are unlikely to be observable, as shown in Figure 1S. Additionally, expanding this
 284 analysis to include more picket fence spectra would help capture the true extent of the
 285 variability in these spectra and further assess the consistency with the parallel electric
 286 field driving mechanism.

287 If parallel electric fields indeed drive picket fence emissions, the structure of the picket
 288 fence constrains the electric field's structure. Under the influence of a parallel electric
 289 field at picket fence altitudes, the EEDF equilibrates in between ~ 0.1 and 50 ms, increas-
 290 ing with altitude (Gurevich, 1978). Given the ~ 0.7 s radiative lifetime of $O(^1S)$ (Itikawa
 291 & Ichimura, 1990), and the several microseconds radiative lifetime of $N_2(B^3\Pi_g)$ (Eyler
 292 & Pipkin, 1983), visible emissions should emerge within 1 s of the parallel electric field
 293 onset, depending on the altitude. While electron transport or neutral winds may induce
 294 some blurring, the emissions should predominantly trace the parallel electric fields. As
 295 a result, the electric fields would exhibit similar structure to the picket fence itself: aligned
 296 in a rayed east/west arc, confined between 97 and 150 km in altitude, and organized along
 297 the local magnetic field (Archer, St.-Maurice, et al., 2019). However, the non-field-aligned
 298 emission ‘streaks’ below the picket fence (103-108 km) may not trace parallel electric fields,
 299 as these are hypothesized to be a consequence of plasma turbulence (Semeter et al., 2020).

300 While this study refrains from speculating on sources or resulting altitude profiles
 301 of parallel electric fields, Lynch et al. (2022) and Mishin and Streltsov (2022) suggest that
 302 parallel electric fields could be the consequence of different ionospheric instabilities driven
 303 by extreme SAIDs. Lynch et al. (2022) suggest that wave electric fields parallel to the
 304 magnetic field, arising from a tearing-mode instability, could drive the picket fence. Al-
 305 though they do not model the magnitude or frequency of these waves, our study's re-
 306 sults are applicable to wave electric fields which vary significantly slower than the EEDF
 307 equilibration timescale. Mishin and Streltsov (2022)'s simulation of the ionospheric feed-
 308 back instability yielded maximum field strengths of ~ 26 mV/m, occurring at 130-140
 309 km. Our predictions achieved the observed N_2 1P to GL emissions ratio for ~ 7 mV/m
 310 electric field strengths at 135 km, showing reasonable agreement with Mishin and Streltsov
 311 (2022)'s results.

312 Parallel electric fields may play a significant role in the ionosphere beyond the picket
 313 fence. In the auroral region, certain optical features share spectral characteristics with
 314 the picket fence and cannot be explained by precipitation. Fragmented aurora-like emis-
 315 sions (FAE) are non-field aligned green patches showing GL and N_2 1P emissions but
 316 lacking N_2^+ 1N (Dreyer et al., 2021). Enhanced aurora (EA) consist of thin, bright lay-
 317 ers within regular aurora, exhibiting increased N_2 1P relative to N_2^+ 1N (Hallinan et al.,
 318 1997). Similar to the picket fence, both FAE and EA are suggested to result from suprather-
 319 mal electron populations locally generated by parallel electric fields or wave-particle in-
 320 teractions (Hallinan et al., 1997; Dreyer et al., 2021). Karlsson et al. (2005) simulated
 321 EA using a simple auroral current model, generating parallel electric fields with max-
 322 imum strength of ~ 30 mV/m peaking between 80-120 km. Collectively, this suggests that
 323 the picket fence might represent one example of a class of aurora-like emissions gener-
 324 ated locally by parallel electric fields, not particle precipitation, although the sources of
 325 these fields may differ. These findings underscore the potential significance of parallel
 326 electric fields. In particular, since visible and ultraviolet auroral observations are increas-
 327 ingly used to trace particle precipitation and infer magnetospheric activity, it is impor-
 328 tant to better understand and quantify other sources of emission beyond particle pre-

329 cipitation. Thus, investigating the prevalence and sources of these parallel electric fields
 330 warrants further attention from the broader scientific community.

331 The most definitive way to verify the existence of these parallel electric fields is with
 332 in situ measurements. While magnetospheric parallel electric fields have long been as-
 333 sociated with auroral particle acceleration and precipitation (Marklund, 1993; Shelley,
 334 1995; Paschmann et al., 2003), static current closure models predict parallel electric fields
 335 from the ionospheric F-region to the E-region to be orders of magnitude weaker than per-
 336 pendicular fields ($\mu\text{V}/\text{m}$ rather than mV/m) (e.g. Farley Jr, 1959). Ionospheric electric
 337 field measurements routinely assume zero parallel electric field when deriving a full vec-
 338 tor perpendicular field from two-dimensional measurements (Pfaff et al., 2021). How-
 339 ever, satellite measurements of enhanced downward currents and modeling of the iono-
 340 spheric response suggest significant parallel fields in the collisional base of the D and E
 341 regions (Marklund et al., 1997; Karlsson & Marklund, 1998), but to our knowledge, no
 342 measurements have probed the existence of these fields. Confirming the existence of these
 343 fields is crucial for advancing our understanding of a wide variety of phenomena in the
 344 auroral and subauroral regions. Based on our study’s results, we propose that attempt-
 345 ing to measure these electric fields in situ should be a priority for the space physics com-
 346 munity.

347 Acknowledgments

348 We express our gratitude to Stephen Mende and John Bonnell for their inspiration
 349 and valuable input in this study. We also acknowledge the University of Colorado Space
 350 Weather Technology, Research and Education Center for providing pyMSIS. Partial sup-
 351 port for this work was provided by NSF grant AGS-2010088 to Pennsylvania State Uni-
 352 versity, NASA grant 80NSSC21K1386 to the University of California, Berkeley, and the
 353 Robert P. Lin Fellowship.

354 Data Availability Statement

355 The TREx data used in this study is available freely from <https://data.phys.ucalgary.ca/>.

356 References

- 357 Archer, W., Gallardo-Lacourt, B., Perry, G. W., St.-Maurice, J.-P., Buchert, S. C.,
 358 & Donovan, E. (2019). Steve: The optical signature of intense subauroral ion
 359 drifts. *Geophys. Res. Lett.*, *46*(12), 6279–6286.
- 360 Archer, W., St.-Maurice, J.-P., Gallardo-Lacourt, B., Perry, G., Cully, C., Donovan,
 361 E., . . . Eurich, D. (2019). The vertical distribution of the optical emissions of
 362 a Steve and Picket Fence event. *Geophys. Res. Lett.*, *46*(19), 10719–10725.
- 363 Bennett, C. L., & Bourassa, N. (2021). Improved analysis of STEVE photographs.
 364 *J. Geophys. Res.: Space Phys.*, *126*(4), e2020JA027843.
- 365 Bilitza, D., Altadill, D., Truhlik, V., Shubin, V., Galkin, I., Reinisch, B., & Huang,
 366 X. (2017). International reference ionosphere 2016: From ionospheric climate
 367 to real-time weather predictions. *Space Weather*, *15*(2), 418–429.
- 368 Chu, X., Malaspina, D., Gallardo-Lacourt, B., Liang, J., Andersson, L., Ma, Q., . . .
 369 others (2019). Identifying STEVE’s magnetospheric driver using conjugate
 370 observations in the magnetosphere and on the ground. *Geophys. Res. Lett.*,
 371 *46*(22), 12665–12674.
- 372 Dreyer, J., Partamies, N., Whiter, D., Ellingsen, P. G., Baddeley, L., & Buchert,
 373 S. C. (2021). Characteristics of fragmented aurora-like emissions (FAEs)
 374 observed on Svalbard. In *Annales Geophysicae* (Vol. 39, pp. 277–288).
- 375 Emmert, J. T., Drob, D. P., Picone, J. M., Siskind, D. E., Jones Jr, M., Mlynczak,
 376 M., . . . others (2021). NRLMSIS 2.0: A whole-atmosphere empirical

- 377 model of temperature and neutral species densities. *Earth Space Sci.*, 8(3),
 378 e2020EA001321.
- 379 Emmert, J. T., Jones Jr, M., Siskind, D. E., Drob, D. P., Picone, J. M., Stevens, M.,
 380 ... others (2022). NRLMSIS 2.1: An empirical model of nitric oxide incorpo-
 381 rated into MSIS. *J. Geophys. Res.: Space Phys.*, 127(10), e2022JA030896.
- 382 Eyler, E., & Pipkin, F. (1983). Lifetime measurements of the $B^3\Pi_g$ state of N_2 using
 383 laser excitation. *J. Chem. Phys.*, 79(8), 3654–3659.
- 384 Farley Jr, D. (1959). A theory of electrostatic fields in a horizontally stratified
 385 ionosphere subject to a vertical magnetic field. *J. Geophys. Res.*, 64(9), 1225–
 386 1233.
- 387 Gallardo-Lacourt, B., Frey, H., & Martinis, C. (2021). Proton aurora and optical
 388 emissions in the subauroral region. *Space Sci. Rev.*, 217, 1–36.
- 389 Gillies, D. M., Donovan, E., Hampton, D., Liang, J., Connors, M., Nishimura, Y., ...
 390 Spanswick, E. (2019). First observations from the TReX spectrograph: The
 391 optical spectrum of STEVE and the picket fence phenomena. *Geophys. Res.*
 392 *Lett.*, 46(13), 7207–7213.
- 393 Gillies, D. M., Liang, J., Gallardo-Lacourt, B., & Donovan, E. (2023). New insight
 394 into the transition from a SAR arc to STEVE. *Geophys. Res. Lett.*, 50(6),
 395 e2022GL101205.
- 396 Gull, S. F. (1989). Bayesian data analysis: Straight-line fitting. In *Maximum*
 397 *Entropy and Bayesian Methods: Cambridge, England, 1988* (pp. 511–518).
 398 Springer.
- 399 Gurevich, A. V. (1978). *Nonlinear Phenomena in the Ionosphere*. New York, NY:
 400 Springer-Verlag.
- 401 Hagelaar, G., & Pitchford, L. C. (2005). Solving the Boltzmann equation to obtain
 402 electron transport coefficients and rate coefficients for fluid models. *Plasma*
 403 *Sources Sci. Technol.*, 14(4), 722.
- 404 Hallinan, T., Kimball, J., Stenbaek-Nielsen, H., & Deehr, C. (1997). Spectroscopic
 405 evidence for suprathermal electrons in enhanced auroras. *J. Geophys. Res.:*
 406 *Space Phys.*, 102(A4), 7501–7508.
- 407 Harding, B. J., Mende, S. B., Triplett, C. C., & Wu, Y.-J. J. (2020). A mech-
 408 anism for the STEVE continuum emission. *Geophys. Res. Lett.*, 47(7),
 409 e2020GL087102.
- 410 Ilma, R. (2017, Jan). rilma/pyiri2016: Official release of the iri2016 wrapper in
 411 python.
 412 doi: 10.5281/zenodo.240895
- 413 Itikawa, Y., & Ichimura, A. (1990). Cross sections for collisions of electrons and pho-
 414 tons with atomic oxygen. *J. Phys. Chem. Ref. Data*, 19(3), 637–651.
- 415 Karlsson, T., & Marklund, G. (1998). Simulations of effects of small-scale auro-
 416 ral current closure in the return current region. *Physics of Space Plasmas*, 15,
 417 401.
- 418 Karlsson, T., Marklund, G., Brenning, N., & Axnäs, I. (2005). On enhanced aurora
 419 and low-altitude parallel electric fields. *Physica Scripta*, 72(5), 419.
- 420 Laher, R. R., & Gilmore, F. R. (1990). Updated excitation and ionization cross sec-
 421 tions for electron impact on atomic oxygen. *J. Phys. Chem. Ref. Data*, 19(1),
 422 277–305.
- 423 Lawton, S., & Phelps, A. (1978). Excitation of the $b^1\Sigma_g^+$ state of O_2 by low energy
 424 electrons. *J. Chem. Phys.*, 69(3), 1055–1068.
- 425 Liang, J., St-Maurice, J., & Donovan, E. (2021). A time-dependent two-dimensional
 426 model simulation of lower ionospheric variations under intense SAID. *J. Geo-*
 427 *phys. Res.: Space Phys.*, 126(12), e2021JA029756.
- 428 Liang, J., Zou, Y., Nishimura, Y., Donovan, E., Spanswick, E., & Conde, M. (2021).
 429 Neutral wind dynamics preceding the STEVE occurrence and their possible
 430 preconditioning role in STEVE formation. *J. Geophys. Res.: Space Phys.*,
 431 126(3), e2020JA028505.

- 432 Lucas, G. (2023, Jan). pynsis.
433 doi: 10.5281/zenodo.7581692
- 434 Lynch, K. A., McManus, E., Gutow, J., Burleigh, M., & Zettergren, M. (2022).
435 An ionospheric conductance gradient driver for subauroral picket fence visi-
436 ble signatures near STEVE events. *J. Geophys. Res.: Space Phys.*, *127*(12),
437 e2022JA030863.
- 438 MacDonald, E. A., Donovan, E., Nishimura, Y., Case, N. A., Gillies, D. M.,
439 Gallardo-Lacourt, B., . . . others (2018). New science in plain sight: Citizen
440 scientists lead to the discovery of optical structure in the upper atmosphere.
441 *Sci. Adv.*, *4*(3), eaaq0030.
- 442 Marklund, G. (1993). Viking investigations of auroral electrodynamical processes. *J.*
443 *Geophys. Res.: Space Phys.*, *98*(A2), 1691–1704.
- 444 Marklund, G., Karlsson, T., & Clemmons, J. (1997). On low-altitude particle ac-
445 celeration and intense electric fields and their relationship to black aurora. *J.*
446 *Geophys. Res.: Space Phys.*, *102*(A8), 17509–17522.
- 447 Martinis, C., Griffin, I., Gallardo-Lacourt, B., Wroten, J., Nishimura, Y., Baum-
448 gardner, J., & Knudsen, D. (2022). Rainbow of the night: First direct ob-
449 servation of a SAR arc evolving into STEVE. *Geophys. Res. Lett.*, *49*(11),
450 e2022GL098511.
- 451 Meier, R. (1991). Ultraviolet spectroscopy and remote sensing of the upper atmo-
452 sphere. *Space Sci. Rev.*, *58*(1), 1–185.
- 453 Mende, S., Harding, B., & Turner, C. (2019). Subauroral green steve arcs: Evidence
454 for low-energy excitation. *Geophys. Res. Lett.*, *46*(24), 14256–14262.
- 455 Michael. (2021, Oct). space-physics/igrf: Robust build, matlab unit test.
456 doi: 10.5281/zenodo.5560949
- 457 Mishin, E., & Streltsov, A. (2022). On the kinetic theory of subauroral arcs. *J. Geo-*
458 *phys. Res.: Space Phys.*, *127*(8), e2022JA030667.
- 459 Morrill, J., Bucsela, E., Pasko, V., Berg, S., Heavner, M., Moudry, D., . . . Sent-
460 man, D. (1998). Time resolved N₂ triplet state vibrational populations and
461 emissions associated with red sprites. *J. Atmos. Sol. Terr. Phys.*, *60*(7-9),
462 811–829.
- 463 Nishimura, Y., Dyer, A., Kangas, L., Donovan, E., & Angelopoulos, V. (2023). Un-
464 solved problems in strong thermal emission velocity enhancement (STEVE)
465 and picket fence. *Front. Astron. Space Sci.*, *10*, 3.
- 466 Nishimura, Y., Gallardo-Lacourt, B., Zou, Y., Mishin, E., Knudsen, D., Donovan, E.,
467 . . . Raybell, R. (2019). Magnetospheric signatures of STEVE: Implications for
468 the magnetospheric energy source and interhemispheric conjugacy. *Geophys.*
469 *Res. Lett.*, *46*(11), 5637–5644.
- 470 Paschmann, G., Haaland, S., Treumann, R., & Treumann, R. A. (2003). *Auroral*
471 *plasma physics* (Vol. 15). Springer Science & Business Media.
- 472 Pfaff, R., Uribe, P., Fourre, R., Kujawski, J., Maynard, N., Acuna, M., . . . others
473 (2021). The vector electric field investigation (VEFI) on the C/NOFS satellite.
474 *Space Sci. Rev.*, *217*, 1–88.
- 475 Phelps, A., & Pitchford, L. (1985). Anisotropic scattering of electrons by N₂ and its
476 effect on electron transport. *Phys. Rev. A*, *31*(5), 2932.
- 477 Picone, J., Hedin, A., Drob, D. P., & Aikin, A. (2002). NRLMSISE-00 empirical
478 model of the atmosphere: Statistical comparisons and scientific issues. *J. Geo-*
479 *phys. Res.: Space Phys.*, *107*(A12), SIA–15.
- 480 Raizer, Y. P. (1991). *Gas Discharge Physics*. New York, NY: Springer-Verlag.
- 481 Semeter, J., Hunnekuhl, M., MacDonald, E., Hirsch, M., Zeller, N., Chernenkoff,
482 A., & Wang, J. (2020). The mysterious green streaks below STEVE. *AGU*
483 *Advances*, *1*(4), e2020AV000183.
- 484 Shelley, E. (1995). The auroral acceleration region: The world of beams, conies,
485 cavitons, and other plasma exotica. *Rev. Geophys.*, *33*(S1), 709–714.

- 486 Shemansky, D. E., & Liu, X. (2005). Evaluation of electron impact excitation of
487 $N_2 X^1\Sigma_g^+(0)$ into the $N_2^+ X^2\Sigma_g^+(v)$, $A^2\Pi_u(v)$, and $B^2\Sigma_u^+(v)$ states. *J. Geophys.*
488 *Res.: Space Phys.*, 110(A7).
- 489 Vallance Jones, A. (1974). *Aurora*. D. Reidel publishing company.
- 490 Wardinski, I., Saturnino, D., Amit, H., Chambodut, A., Langlais, B., Manda, M.,
491 & Thebault, E. (2020). Geomagnetic core field models and secular variation
492 forecasts for the 13th International Geomagnetic Reference Field (IGRF-13).
493 *Earth, Planets and Space*, 72(1), 1–22.
- 494 Yadav, S., Shiokawa, K., Otsuka, Y., Connors, M., & St Maurice, J.-P. (2021).
495 Multi-wavelength imaging observations of STEVE at Athabasca, Canada. *J.*
496 *Geophys. Res.: Space Phys.*, 126(2), 2020JA028622.
- 497 Yonker, J. D., & Bailey, S. M. (2020). $N_2(A)$ in the terrestrial thermosphere. *J.*
498 *Geophys. Res.: Space Phys.*, 125(1), e2019JA026508.